An Optimal Variable Frequency Phase Shift Control Strategy for ZVS Operation Within Wide Power Range in IPT Systems

Hongsheng Hu, Tao Cai, Shanxu Duan, *Senior Member, IEEE*, Xiaoming Zhang, Jintao Niu, and Hao Feng, *Member, IEEE*

***Abstract*—In inductive power transfer (IPT) systems, zero-voltage-switching (ZVS) operation within wide power range is an urgent requirement to improve system efficiency and reduce electromagnetic interference. The combination of phase shift (PS) control and variable frequency control is usually adopted to realize ZVS operation. However, in inductor-capacitor-capacitor-series (*LCC*-S) systems, the abovementioned hybrid strategy cannot be used directly due to nonnegligible harmonics, which result in detection difficulties or imprecise calculation of turn-OFF current. To solve this problem, this article proposes an optimal variable frequency phase shift (VFPS) control strategy for *LCC*-S systems to realize ZVS operation within wide power range. The universal harmonic-considered time-domain model of *LCC*-S system is deduced, and thus, the switching-moment current of power switches can be calculated accurately. Based on this value, an optimal working trajectory for ZVS operation with minimum frequency variation is presented. Finally, a 2.2-kW IPT prototype is built up to verify the universality of the deduced model and the validity of the proposed optimal VFPS control. Compared with PS control and the VFPS control based on fundamental-harmonic-approximation method, the systems realizes ZVS operation under wide power range with efficiency increase of 2.6%–6.9% and 0.8%–8.8%, respectively, and a peak efficiency of 96.4% is achieved.**

***Index Terms*—Inductive power transfer (IPT), zero-voltage-switching (ZVS), wide power range, variable frequency phase shift (VFPS), time domain model.**

I. Introduction

INDUCTIVE power transfer (IPT) technology is gaining more and more attentions due to its convenience and safety in recent years, and it is widely applied in biomedical implants [1], [2], consumer electronics [3]–[6], underwater loads [7]–[9], electrical vehicles [10]–[15], etc.

Manuscript received April 21, 2019; revised August 14, 2019; accepted October 2, 2019. Date of publication October 13, 2019; date of current version February 11, 2020. This work was supported by the National Key Research and Development Program of China by MOST (Key technologies of high performance charger for electric vehicles based on advanced power semiconductors) under Grant 2018YFB0106300. Recommended for publication by Associate Editor S. Williamson. *(Corresponding author: Tao Cai.)*

The authors are with the State Key Laboratory of Advanced Electromagnetic Engineering and Technology, School of Electrical and Electronic Engineering, Huazhong University of Science and Technology, Wuhan 430074, P.R. China (e-mail: huhongsheng@hust.edu.cn; caitao@hust.edu.cn; duanshanxu@hust.edu.cn; xiaomingzhang@hust.edu.cn; jt_niu@hust.edu.cn; hfeng6@ncsu.edu).

Color versions of one or more of the figures in this article are available online at http://ieeexplore.ieee.org.

Digital Object Identifier 10.1109/TPEL.2019.2947092

In IPT systems, the power range needs to be wide enough for different working conditions. During the process of power regulation, zero-voltage-switching (ZVS) operation is necessary for improving system efficiency [16], [17] and reducing electromagnetic interference [18], [19]. Thus, the ZVS operation within wide power range is required.

So far, numerous control strategies of full-bridge (F-B) inverters in IPT systems have been studied to transfer power efficiently, which can be divided into following four major types.

1) Variable pulsewidth control, including symmetrical pulsewidth control such as phase shift (PS) control [20], [21], asymmetrical pulsewidth control such as asymmetrical duty-cycle (ADC) control [22], [23], and asymmetrical voltage cancellation (AVC) control [24], [25], adjusts the pulsewidth of the F-B inverter to control output voltage or power. However, when only adopting variable pulsewidth control, IPT systems cannot achieve ZVS operation with large variations of load resistance or output power [25], which results in large voltage spikes in the output voltage of the inverter and leads to a low efficiency.
2) Variable frequency (VF) control [26], [27], adjusts the switching frequency of the F-B inverter according to output power. However, in IPT systems, a wide range of frequency variation will result in poor transfer efficiency and wide noise spectrum especially in light load condition [28].
3) Pulse density control [29], [30] repeats alternate run and stop to adjust the average output power. A traditional pulse density modulation was used in [29] to achieve ZVS and zero-current switching. However, this method causes severe output current fluctuation.
4) VF variable pulse-width control [18], [28], [31]–[33], especially variable frequency phase shift (VFPS) control, features with two degrees of freedom (DOF), i.e., the PS angle and the switching frequency. The PS angle is used to regulate the output voltage or power, and the switching frequency is used to realize ZVS operation within wide power range. Thus, compared with other three methods mentioned above, it is common and practical.

Recently, several research works have been conducted on the VFPS control, and the obtainment of the turn-OFF current is the key topic since it directly relates to the ZVS condition. For simple compensation topologies such as series–series topology,

the turn-OFF current can be obtained easily by detection or calculation, then the switching frequency of the F-B inverter is adjusted to realize ZVS operation. In [18], an enhanced phase detection methodology was proposed to measure the phase of turn-OFF current, and based on it, an optimal operation frequency range was put forward in [28]. The multiple harmonics analysis (MHA) was developed in [31], where the turn-OFF current expression of power switches was acquired, and new phenomena in ZVS and voltage gain were discovered consequently. Moreover, the pulsewidth modulation phase-locked-loop control strategy was proposed in [32] to achieve output voltage control and ZVS operation at the same time.

However, for complicated compensation topologies, especially the multiple resonant component network inductor-capacitor-capacitor-series (*LCC*-S) topology that is commonly used due to the constant current characteristic in primary coil, the turn-OFF current of the F-B inverter contains numerous harmonics, which increases the detection difficulty and calculation complexity. More specifically, for detection, Kim *et al*. [10] proposed a zero phase angle tracking and PS control to correspond the output voltage increment caused by high coupling coefficient. However, the detection issues such as detection error and multiple zero crossing points of turn-OFF current under light load increased its implementation difficulty. For calculation, the harmonic influence on the instantaneous turn-OFF current should be considered for precise results [34]. The MHA in [31] cannot be used directly in *LCC*-S topology, because the time-domain expression of turn-OFF current contains infinite items, which leads to the difficulty of calculating the turn-OFF current. Zhang *et al*. [34] proposed a closed-form expression of turn-OFF current in double-side *LCC* compensation topology for bidirectional IPT system, and based on it, the instantaneous current at switching moments can be calculated accurately. However, the time-domain model proposed in [34] and [35] was not universal and cannot be applied in variable-frequency control. Generally, there is no universal time-domain and closed-form model of *LCC*-S topology, which is necessary for different control strategies.

To realize ZVS operation within wide power range, an optimal VFPS control strategy suitable for the widely used *LCC*-S IPT system is proposed for the first time. The main contributions of this article are as follows.

1) The harmonic-considered universal time-domain model of *LCC*-S topology is proposed for the first time, and the closed-form expression of MOSFET current is also derived, which can be used to obtain the key turn-OFF current accurately and is suitable for both variable width control and VF control.
2) With the calculated turn-OFF current, the optimal VFPS control strategy applied on *LCC*-S IPT system is proposed, with which the ZVS operation can be realized within wide power range. In addition, the frequency deviation (between the switching frequency and resonant frequency) is minimum, which ensures high efficiency of the inverter and the resonant tank. This strategy is universal in *LCC*-S IPT system.

The rest of this article is organized as follows. In Section II, the impedance characteristics of *LCC*-S topology under the *N*th harmonic are analyzed. In Section III, the harmonic-considered universal time-domain model is deduced, and the closed-form expression of instantaneous turn-OFF current is obtained. In Section IV, the optimal VFPS control strategy is put forward to realize ZVS operation within wide power range. In Section V, a 2.2-kW IPT prototype is built up to verify the universality of the deduced model and the validity of the proposed control strategy, and the conclusion is given in Section VI.

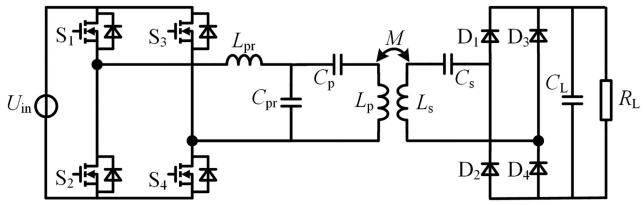

Fig. 1. LCC-S compensated IPT topology.

II. Impedance Characteristics of *LCC*-S Topology Under the *N*th Harmonic

The instantaneous turn-OFF current of the F-B inverter is the assessment criteria of ZVS operation. However, in *LCC*-S topology, this current contains numerous harmonics and, thus, cannot be calculated precisely with the common fundamental harmonic approximation (FHA) method. For convenient analysis of turn-OFF current, two important premises of *LCC*-S topology and their derivative process are analyzed in this section.

Fig. 1 shows the typical circuit diagram of the *LCC*-S compensated IPT topology. $U_{\rm in}$ is the input dc voltage of the primary F-B inverter. S_1–S_4 are the power switches of the primary-side F-B inverter. L_{pr} is the series compensated inductance. C_{pr} is the parallel compensated capacitor. C_p and C_s are the series compensated capacitors of primary side and secondary side, respectively. L_p and L_s are the self-inductances of transmitter and receiver coils, respectively. M is the mutual inductance between coils. D_1–D_4 are the secondary-side rectifier diodes. C_L is the secondary dc capacitor, and R_L is the load resistance.

In Fig. 1, the resonant frequency and switching frequency have following relations:

$$\begin{cases} \omega_n = 2\pi f_n \\ \omega_s = 2\pi f_s = \frac{2\pi}{T_s} \end{cases} \tag{1}$$

where ω_n and f_n are resonant angular frequency and resonant frequency of *LCC*-S compensation topology, respectively; ω_s, f_s, and T_s are switching angular frequency, switching frequency, and switching period of the F-B inverter, respectively.

In order to minimize the input reactive current and improve system efficiency, the input impedance of primary-side network should be resistive, and thus, the design principles of parameters in *LCC*-S topology are given as

$$\begin{cases} \omega_s L_{pr} = \frac{1}{\omega_s C_{pr}} \\ \omega_s L_p = \omega_s L_{pr} + \frac{1}{\omega_s C_p} \\ \omega_s L_s = \frac{1}{\omega_s C_s}. \end{cases} \tag{2}$$

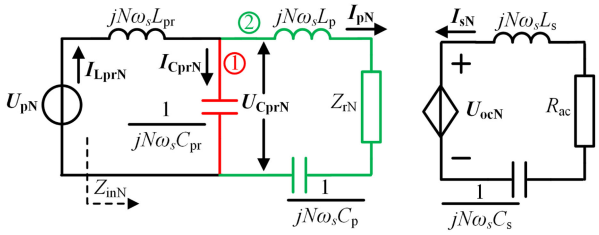

Fig. 2. Equivalent circuit under the excitation of $\boldsymbol{U_{pN}}$.

TABLE I
MAIN PARAMETERS OF THE *LCC*-S SYSTEM

Symbol	Value	Symbol	Value
L_{pr}	24.9uH	C_{pr}	143.7nF
L_p	92uH	C_p	52.3nF
L_s	87.8uH	C_s	40nF
f_s	85kHz	R_{ac}	21.2Ω

The quality factor Q_{Load} is defined as $Q_{\text{Load}} = \sqrt{L_s/C_s}//R_{\text{ac}}$. To simplify the analysis of *LCC*-S topology, the F-B inverter and the rectifier together with R_L are equivalent to a voltage source and a resistive load, respectively. The equivalent circuit of Fig. 1 under *N*th harmonic can be obtained as shown in Fig. 2.

In Fig. 2, the subscript *N* ($N = 1, 2, 3, \ldots$) is the harmonic order of signals. $\boldsymbol{U_{pN}}$ is the equivalent input voltage of primary resonant network; $Z_{\text{in}N}$ is the input impedance observing from primary side; $\boldsymbol{I_{LprN}}$ is the input current flowing through L_{pr}; $\boldsymbol{I_{CprN}}$ is the current flowing through C_{pr}; $\boldsymbol{U_{CprN}}$ is the voltage of C_{pr}; $\boldsymbol{I_{pN}}$ and $\boldsymbol{I_{sN}}$ are the coil currents of the primary and secondary sides, respectively; Z_{rN} is the reflected impedance; $\boldsymbol{U_{ocN}}$ is the open-circuit voltage of secondary side; R_{ac} is the equivalent resistance of the output rectification network together with the load R_L, and $R_{\text{ac}} = 8/(\pi^2 R_L)$. The impedances of branch 1 (namely Z_{branch1}) and 2 (namely Z_{branch2}) in Fig. 2 can be expressed and simplified as follows:

$$\begin{cases} Z_{\text{branch1}} = \frac{1}{jN\omega_s C_{pr}} \\ Z_{\text{branch2}} = jN\omega_s L_p + \frac{1}{jN\omega_s C_p} + Z_{rN} \\ \qquad\qquad \approx j\frac{N^2\omega_s^2 L_p C_p - 1}{N\omega_s C_p}, \qquad N \geq 2 \end{cases} \tag{3}$$

where

$$Z_{rN} = \frac{(N\omega_s M)^2}{jN\omega_s L_s + \frac{1}{jN\omega_s C_s} + R_{\text{ac}}} \approx -k^2 jN\omega_s L_p. \tag{4}$$

In (4), $M = k\sqrt{L_p L_s}$ and k is the coupling coefficient. The impedance of inductor is N^2 times larger than the one of capacitor under *N*th harmonic when inductor and capacitor are full compensated under fundamental frequency. The range of k is normally [0.1–0.3], which means that Z_{rN} is very small compared with $jN\omega_s L_p$, and thus, Z_{branch2} can be simplified to (3).

Combining (2) and (3), the relation between Z_{branch1} and Z_{branch2} can be acquired as

$$Z_{\text{branch1}} \approx \frac{C_p}{N^2{\omega_s}^2 L_p C_{pr} C_p - C_{pr}} Z_{\text{branch2}}, N \geq 2. \tag{5}$$

In order to investigate harmonic content, the fundamental component is taken as the reference. For fundamental frequency, Z_{in1} and $\boldsymbol{U_{p1}}$ can be obtained as follows according to (2):

$$\begin{cases} Z_{\text{in1}} = (\omega_s L_{pr})^2 / R_{\text{ac}} \\ \boldsymbol{U_{p1}} = U_{\text{in}} 2\sqrt{2}/\pi. \end{cases} \tag{6}$$

For *N*th harmonic, $Z_{\text{in}N}$ and $\boldsymbol{U_{pN}}$ can be similarly derived as (7), where $Z_{\text{in}N}$ is simplified based on (5)

$$\begin{cases} Z_{inN} = jN\omega_s L_{pr} + (Z_{\text{branch1}}//Z_{\text{branch2}}) \\ \qquad\qquad \approx jN\omega_s L_{pr} + Z_{\text{branch1}} = \left(\frac{N^2-1}{N}\omega_s L_{pr}\right) j, \quad N \geq 2 \\ \boldsymbol{U_{pN}} = \frac{U_{\text{in}} 2\sqrt{2}}{N\pi}. \end{cases} \tag{7}$$

Based on (6) and (7), it can be known that for fundamental frequency, Z_{in1} is resistive, and thus, $\boldsymbol{I_{Lpr1}}$ and $\boldsymbol{U_{p1}}$ are in the same phase; for *N*th harmonic, $Z_{\text{in}N}$ is inductive and, thus, $\boldsymbol{I_{LprN}}$ lags behind $\boldsymbol{U_{pN}}$ 90°. To describe the harmonic content in $\boldsymbol{I_{Lpr}}$, define Δ as the ratio between $\sum_{N=2}^{\infty} |\boldsymbol{I_{LprN}}|$ and $|\boldsymbol{I_{Lpr1}}|$, and the expression of Δ is given as

$$\begin{aligned} \Delta &= \frac{\sum_{N=2}^{\infty} |\boldsymbol{I_{LprN}}|}{|\boldsymbol{I_{Lpr1}}|} = \frac{\omega_s L_{pr}}{R_{\text{ac}}} \sum_{N=2}^{\infty} \frac{1}{N^2 - 1} \\ &= \frac{\omega_s L_{pr}}{2R_{\text{ac}}} \lim_{N\to\infty} \left(\frac{N}{N+1}\right) \approx \frac{\omega_s L_{pr}}{2R_{\text{ac}}}. \end{aligned} \tag{8}$$

In (8), the orders of magnitude of $\omega_s L_{pr}$ and R_{ac} are close, which means that $\sum_{N=2}^{\infty} |\boldsymbol{I_{LprN}}|$ and $|\boldsymbol{I_{Lpr1}}|$ are similar sized. Thus, $\boldsymbol{I_{Lpr}}$ contains numerous harmonics. To verify the above analysis, the parameters in Table I are substituted into (8) as an example, and Δ is obtained as 0.313, reflecting that the harmonics in $\boldsymbol{I}_{Lpr}$ are nonnegligible.

Similarly, in order to compare the harmonic voltage $\boldsymbol{U_{CprN}}$ and the fundamental voltage $\boldsymbol{U_{Cpr1}}$ in C_{pr}, define Γ_N as the ratio between them. Based on Fig. 2 and (7), the expression of Γ_N is given as

$$\begin{aligned} \Gamma_N &= \frac{|\boldsymbol{U_{CprN}}|}{|\boldsymbol{U_{Cpr1}}|} = \frac{\left|\frac{\boldsymbol{U_{pN}}}{Z_{\text{in}N}} (Z_{\text{branch1}}//Z_{\text{branch2}})\right|}{\left|\frac{\boldsymbol{U}_{p1}}{j\omega_s L_{pr}} \left(j\omega_s L_p + \frac{1}{j\omega_s C_p} + Z_r\right)\right|} \\ &\approx \frac{|\boldsymbol{U_{pN}}| \frac{1}{N^2-1}}{|\boldsymbol{U_{p1}}| \left|1 + \frac{Z_r}{j\omega_s L_{pr}}\right|} \leq \frac{1}{N(N^2-1)}, \quad N \geq 2. \end{aligned} \tag{9}$$

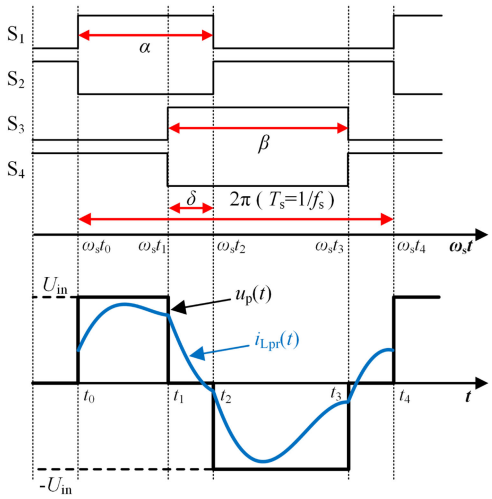

Fig. 3. Typical waveforms of the F-B inverter.

According to (9), it is easy to know that Γ_N decreases with N increasing. Therefore, it can be known that $|\boldsymbol{U_{CprN}}|$ is much smaller than $|\boldsymbol{U_{Cpr1}}|$ when N is big. Similarly taking parameters in Table I as an example, when $N = 4$, Γ_N is smaller than 0.017 and, thus, $|\boldsymbol{U_{CprN}}|$ is ignorable.

Thus, according to the analysis above, when calculating the turn-OFF current, two following vital premises of *LCC*-S topology can be concluded:

1) the harmonics in $\boldsymbol{I_{Lpr}}$ are nonnegligible;
2) only the fundamental second and third harmonics in $\boldsymbol{U_{Cpr}}$ should be considered.

III. Harmonic-Considered Universal Time-Domain Model of *LCC*-S Compensated IPT Systems

Based on the two premises in Section II, the harmonic-considered universal time-domain model is explained in this section. According to premise 1), the harmonics in $\boldsymbol{I_{Lpr}}$ are nonnegligible, and the corresponding expression can be derived by integrating the voltage of L_{pr} (namely $\boldsymbol{U_{Lpr}}$) in time domain. According to Fig. 2, the time-domain relation between $\boldsymbol{I_{Lpr}}$ and $\boldsymbol{U_{Lpr}}$ is obtained as

$$u_{L_{pr}}(t) = u_p(t) - u_{C_{pr}}(t) = L_{pr}\frac{di_{L_{pr}}(t)}{dt} \tag{10}$$

where $u_p(t)$, $u_{Lpr}(t)$, $u_{Cpr}(t)$, and $i_{Lpr}(t)$ are the time-domain functions of $\boldsymbol{U_p}$, $\boldsymbol{U_{Lpr}}$, $\boldsymbol{U_{Cpr}}$, and $\boldsymbol{I_{Lpr}}$, respectively. According to (10), it can be known that $i_{Lpr}(t)$ can be acquired if $u_p(t)$ and $u_{Cpr}(t)$ are known.

A. Derivation of $u_p(t)$

Based on driving signals of primary power switches and the input voltage of the F-B inverter, $u_p(t)$ can be acquired.

To show the generality of the time-domain model proposed in this article, the universal waveforms of the F-B inverter are given in Fig. 3. It can be seen that there are four DOF, i.e., the switching frequency f_s, the complementary pulsewidth α of S_1 and S_2, the complementary pulsewidth β of S_3 and S_4, and the phase δ of S_4 leading S_1. Based on Fig. 3, the piecewise expression of $u_p(t)$ can be obtained as

$$u_p(t) = \begin{cases} U_{\text{in}}, & t_0 \le t \le t_1 \\ 0, & t_1 \le t \le t_2 \\ -U_{\text{in}}, & t_2 \le t \le t_3 \\ 0, & t_3 \le t \le t_4 \end{cases} \tag{11}$$

where t_0–t_4 are the turn-ON and turn-OFF moments of power switches, and they can be acquired by

$$\begin{cases} \omega_s t_0 = 0 \\ \omega_s t_1 = \alpha - \delta \\ \omega_s t_2 = \alpha \\ \omega_s t_3 = \alpha + \beta - \delta \\ \omega_s t_4 = 2\pi. \end{cases} \tag{12}$$

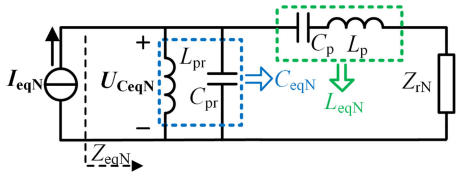

Fig. 4. Primary-side equivalent circuit under the excitation of $\boldsymbol{U_{pN}}$.

B. Derivation of $u_{cpr}(t)$

$u_{Cpr}(t)$ can be obtained based on premise 2) in Section II. Taking $\omega_s t_0$ as the phase reference, the vector form of $\boldsymbol{U_{CprN}}$ is given as (13), where only fundamental second and third harmonics are considered

$$\boldsymbol{U_{CprN}} = |\boldsymbol{U_{CprN}}|\angle\varphi_{U_{CprN}}, \quad N = 1, 2, 3 \tag{13}$$

where $|\boldsymbol{U_{CprN}}|$ and φ_{CprN} are the rms voltage and phase of $\boldsymbol{U_{CprN}}$, respectively.

In order to get $|\boldsymbol{U_{CprN}}|$ and φ_{CeqN}, Fig. 2 is further simplified as Fig. 4 based on the Thevenin–Norton theorem, where $\boldsymbol{I}_{eqN}$ is the equivalent input current source. Z_{eqN} is the equivalent input impedance. C_{eqN} and L_{eqN} are the equivalent capacitor combined with L_{pr} and C_{pr}, and the equivalent inductance combined with L_p and C_p under the Nth harmonic, respectively. They can be expressed as

$$\boldsymbol{I}_{eqN} = \frac{\boldsymbol{U_{pN}}}{jN\omega_s L_{pr}} \tag{14}$$

$$\begin{cases} C_{eqN} = \dfrac{N^2\omega_s^2 L_{pr}C_{pr} - 1}{N^2\omega_s^2 L_{pr}} \\ L_{eqN} = \dfrac{N^2\omega_s^2 C_p L_p - 1}{N^2\omega_s^2 C_p}. \end{cases} \tag{15}$$

According to Fig. 4, $\boldsymbol{U_{CprN}}$ is also the voltage of $C_{\mathrm{eq}N}$, and it can be shown as

$$\boldsymbol{U}_{\boldsymbol{C_{prN}}} = \boldsymbol{U}_{\boldsymbol{C}_{\mathrm{eq}N}} = \boldsymbol{I}_{\mathrm{eq}N} Z_{\mathrm{eq}N} = \left|\boldsymbol{U_{CprN}}\right| \angle \varphi_{U_{CprN}}, \quad N = 1, 2, 3 \tag{16}$$

and $\left|\boldsymbol{U_{CprN}}\right|$ and $\varphi_{C\mathrm{eq}N}$ are

$$\begin{cases} \left|\boldsymbol{U_{CprN}}\right| = \sqrt{\left[\mathrm{Re}\left(\boldsymbol{U}_{\boldsymbol{C}_{\mathrm{eq}N}}\right)\right]^2 + \left[\mathrm{Im}\left(\boldsymbol{U}_{\boldsymbol{C}_{\mathrm{eq}N}}\right)\right]^2} \\ \varphi_{U_{CprN}} = \varphi_N + \arctan\frac{\mathrm{Im}\left(\boldsymbol{U}_{\boldsymbol{C}_{\mathrm{eq}N}}\right)}{\mathrm{Re}\left(\boldsymbol{U}_{\boldsymbol{C}_{\mathrm{eq}N}}\right)} \end{cases} \tag{17}$$

where

The unknown $\left|\boldsymbol{U_{pN}}\right|$ and φ_N can be derived based on the Fourier series of $u_p(t)$ as

$$u_p(t) = a_0 + \sum_{N=1}^{\infty} \sqrt{2}\left|\boldsymbol{U_{pN}}\right| \sin\left(N\omega_s t + \varphi_N\right) \tag{19}$$

$$\begin{cases} \left|\boldsymbol{U_{pN}}\right| = \sqrt{\frac{a_N^2 + b_N^2}{2}} \\ \varphi_N = \arctan\frac{a_N}{b_N} \end{cases} \tag{20}$$

where

$$\begin{cases} a_0 = \frac{1}{T_s}\int_{t_0}^{t_0+T_s} u_p(t)\,dt = \frac{\alpha-\beta}{2\pi} V_{\mathrm{in}} \\ a_N = \frac{2}{T_s}\int_{t_0}^{t_0+T_s} u_p(t)\cos\left(N\omega_s t\right) dt \\ \quad = \frac{V_{\mathrm{in}}}{N\pi}\left[\begin{array}{l} \sin\left(N\left(\alpha-\delta\right)\right) \\ +\sin\left(N\alpha\right) - \sin\left(N\left(\alpha+\beta-\delta\right)\right) \end{array}\right] \\ b_N = \frac{2}{T_s}\int_{t_0}^{t_0+T_s} u_p(t)\sin\left(N\omega_s t\right) dt \\ \quad = \frac{V_{\mathrm{in}}}{N\pi}\left[\begin{array}{l} 1-\cos\left(N\left(\alpha-\delta\right)\right) \\ +\cos\left(N\left(\alpha+\beta-\delta\right)\right) - \cos\left(N\alpha\right) \end{array}\right]. \end{cases} \tag{21}$$

As a result, combining (16)–(21), the time-domain expression of $u_{Cpr}(t)$ can be obtained as

$$u_{Cpr}(t) = \sum_{N=1}^{3}\left[\sqrt{2}\left|\boldsymbol{U_{CprN}}\right| \sin\left(N\omega_s t + \varphi_{U_{CprN}}\right)\right] + a_0 \tag{22}$$

where a_0 is the dc component of $u_{Cpr}(t)$ in (20).

$$\mathrm{Re}Z_{rN} = \frac{\frac{\left(N\omega_s M\right)^2}{Q_{\mathrm{Load}}}\sqrt{\frac{L_s}{C_s}}}{\frac{1}{{Q_{\mathrm{Load}}}^2}\frac{L_s}{C_s} + \left[\frac{\left(N^2\omega_s^2 L_s C_s - 1\right)}{N\omega_s C_s}\right]^2} \quad \mathrm{Im}\ Z_{rN} = -\frac{\left(N\omega_s M\right)^2\left(\frac{N^2\omega_s^2 L_s C_s - 1}{N\omega_s C_s}\right)}{\frac{1}{{Q_{\mathrm{Load}}}^2}\frac{L_s}{C_s} + \left[\frac{\left(N^2\omega_s^2 L_s C_s - 1\right)}{N\omega_s C_s}\right]^2}$$

$$\mathrm{Re}\left(\boldsymbol{U}_{\boldsymbol{C}_{\mathrm{eq}N}}\right) = \frac{\left(N\omega_s L_{eq} + \mathrm{Im}\left(Z_{rN}\right)\right)\left(1 - N^2\omega_s^2 C_{eq} L_{eq} - N\omega_s C_{eq}\mathrm{Im}\left(Z_{rN}\right)\right) - N\omega_s C_{eq}\mathrm{Re}(Z_{rN})^2}{\left[\left(1 - N^2\omega_s^2 C_{eq} L_{eq} - N\omega_s C_{eq}\mathrm{Im}\left(Z_{rN}\right)\right)^2 + \left(N\omega_s C_{eq}\mathrm{Re}\left(Z_{rN}\right)\right)^2\right] N\omega_s L_{pr}}\left|\boldsymbol{U_{pN}}\right|$$

$$\mathrm{Im}\left(\boldsymbol{U}_{\boldsymbol{C}_{\mathrm{eq}N}}\right) = -\frac{\mathrm{Re}Z_{rN}}{\left[\left(1 - N^2\omega_s^2 C_{eq} L_{eq} - N\omega_s C_{eq}\mathrm{Im}\left(Z_{rN}\right)\right)^2 + \left(N\omega_s C_{eq}\mathrm{Re}\left(Z_{rN}\right)\right)^2\right] N\omega_s L_{pr}}\left|\boldsymbol{U_{pN}}\right| \tag{18}$$

$$i_{Lpr}(t) = \begin{cases} \frac{1}{\omega_s L_{pr}}\left\{\left(U_{\mathrm{in}} - a_0\right)\omega_s t + \sum_{N=1}^{3}\left[\begin{array}{l} \frac{\sqrt{2}\mathrm{Re}U_{C_{\mathrm{eq}N}}}{N}\cos\left(N\omega_s t + \varphi_N\right) \\ -\frac{\sqrt{2}\mathrm{Im}U_{C_{\mathrm{eq}N}}}{N}\sin\left(N\omega_s t + \varphi_N\right) \end{array}\right]\right\} + d_0, & t_0 \le t \le t_1 \\ \frac{1}{\omega_s L_{pr}}\left\{-a_0\omega_s t + \sum_{N=1}^{3}\left[\begin{array}{l} \frac{\sqrt{2}\mathrm{Re}U_{C_{\mathrm{eq}N}}}{N}\cos\left(N\omega_s t + \varphi_N\right) \\ -\frac{\sqrt{2}\mathrm{Im}U_{C_{\mathrm{eq}N}}}{N}\sin\left(N\omega_s t + \varphi_N\right) \end{array}\right]\right\} + d_1, & t_1 \le t \le t_2 \\ \frac{1}{\omega_s L_{pr}}\left\{-\left(U_{\mathrm{in}} + a_0\right)\omega_s t + \sum_{N=1}^{3}\left[\begin{array}{l} \frac{\sqrt{2}\mathrm{Re}U_{C_{\mathrm{eq}N}}}{N}\cos\left(N\omega_s t + \varphi_N\right) \\ -\frac{\sqrt{2}\mathrm{ImU}_{\mathrm{C_{eqN}}}}{N}\sin\left(N\omega_s t + \varphi_N\right) \end{array}\right]\right\} + d_2, & t_2 \le t \le t_3 \\ \frac{1}{\omega_s L_{pr}}\left\{-a_0\omega_s t + \sum_{N=1}^{3}\left[\begin{array}{l} \frac{\sqrt{2}\mathrm{Re}U_{C_{\mathrm{eq}N}}}{N}\cos\left(N\omega_s t + \varphi_N\right) \\ -\frac{\sqrt{2}\mathrm{Im}U_{C_{\mathrm{eq}N}}}{N}\sin\left(N\omega_s t + \varphi_N\right) \end{array}\right]\right\} + d_3, & t_3 \le t \le t_4 \end{cases} \tag{23}$$

C. Derivation of $i_{pr}(t)$

Since the time-domain expressions of $u_p(t)$ in (11) and $u_{Cpr}(t)$ in (22) have been derived, by substituting them into (10), the universal expression of $i_{Lpr}(t)$ can be acquired as follows: where d_0–d_3 are constant terms of each piecewise function and determined by circuit parameters. It is noticed that the physical meaning of N in (23) shown as the bottom of the pervious page is the harmonic order considered in $u_{Cpr}(t)$. Besides, all of the harmonics in turn-OFF current are considered in this article. In (23), $|\boldsymbol{U_{CprN}}|$, φ_{CprN}, and a_0 can be obtained by (17) and (21), while d_0–d_3 are unknown. Thus, to acquired $i_{Lpr}(t)$, d_0–d_3 need to be known first.

Due to the continuity of inductance current, the piecewise function (23) should be end to end, and d_0–d_3 have relations as

$$\begin{cases} d_1 = d_0 + \dfrac{U_{\text{in}}}{\omega_s L_{pr}}(\alpha - \delta) \\ d_2 = d_1 + \dfrac{U_{\text{in}}\omega_s t_2}{\omega_s L_{pr}} = \dfrac{U_{\text{in}}}{\omega_s L_{pr}}(2\alpha - \delta) + d_0 \\ d_3 = d_2 - \dfrac{U_{\text{in}}\omega_s t_3}{\omega_s L_{pr}} = \dfrac{U_{\text{in}}}{\omega_s L_{pr}}(\alpha - \beta) + d_0. \end{cases} \tag{24}$$

Because C_p and C_{pr} have the ability of blocking dc component, the integration of $i_{Lpr}(t)$ in (23) over a period T_s equals to zero

$$\int_{t_0}^{t_4} i_{Lpr}(t)\, dt = 0. \tag{25}$$

By combining (23) and (25), the value of d_0 is acquired as

$$d_0 = \frac{U_{\text{in}}\left((\alpha+\beta-\delta)^2 + 2\pi(\alpha-\beta) - (\delta-\alpha)^2 - \alpha^2\right)}{-4\omega_s L_{pr}\pi}. \tag{26}$$

Thus, d_0–d_3 can be obtained by (24) and (26).

As a result, the precise time-domain expression of $i_{Lpr}(t)$ is derived, which considers the influence of harmonics. Besides, it can not only be used in asymmetrical and symmetrical pulse systems, but also in VF systems. In this article, based on (23), the ZVS operation within wide power range can be further studied.

IV. Proposed Optimal VFPS Control

Based on the closed-form expression of $i_{Lpr}(t)$ in (23), the optimal VFPS control strategy featured with minimum frequency variation for *LCC*-S topology is proposed in this section.

The basic principle is to utilize the PS angle δ to control the transmission power P_L and adjust the switching frequency f_s base on $i_{Lpr}(\omega_s t_0)$ derived by (23) to realize ZVS operation. Besides, the frequency variation needs to be minimum for high efficiency within wide power range.

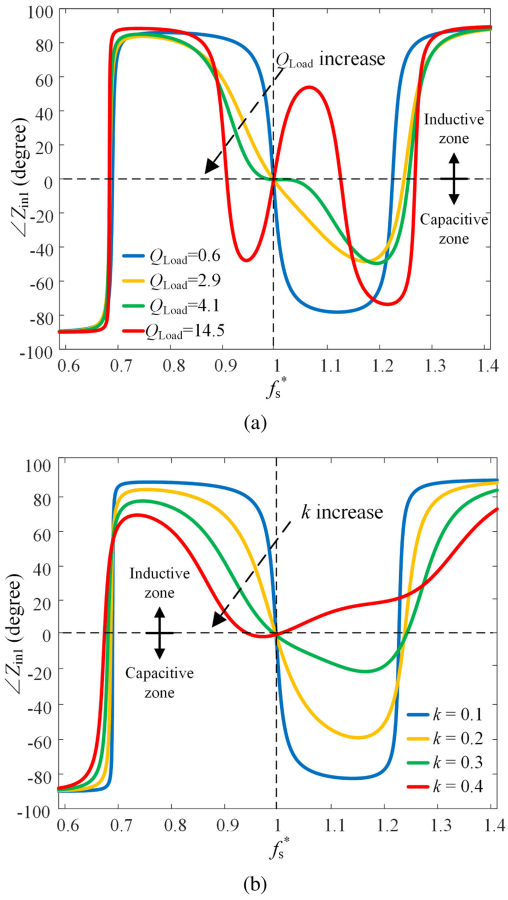

Fig. 5. Relation between $\angle Z_{\text{in1}}$ and f_s^*. (a) Under different Q_{Load}. (b) Under different k.

A. Analysis of Frequency Bifurcation

In order to guarantee the stability of the proposed optimal VFPS control, the phenomenon of frequency bifurcation should be analyzed first. The impedance angle of Z_{in1} under fundamental frequency in Fig. 2 is derived as, (27) shown at the bottom of this page, where L_{eq1}, $\text{Im}(Z_{r1})$, and $\text{Re}(Z_{r1})$ can be calculated from (15) and (18) shown at the bottom of the pervious page, respectively, with $N = 1$. The characteristic curves of impedance angle $\angle Z_{\text{in1}}$ are shown in Fig. 5, where Fig. 5(a) presents the influence of f_s^* and R_L when k is assumed as 0.22; Fig. 5(b) presents the influence of f_s^* and k when R_L is assumed as 26.2 Ω. The superscript "$*$" of f_s^* stands for per-unit value ($f_s = f_n$ is taken as the reference).

As can be seen in Fig. 5(a), when R_L decreases to a low value, the phenomenon of frequency bifurcation will occur around f_n, which is not desirable in VF systems. Similarly, in Fig. 5(b), when k increases to a large value, the frequency bifurcation

$$\angle Z_{\text{in1}} = \arctan \frac{\left\{ \begin{array}{r} [\omega_s L_{\text{eq1}} + \text{Im}(Z_{r1})]\,[1 - \omega_s C_{pr}(\omega_s L_{\text{eq1}} + \text{Im}(Z_{r1}))] - \omega_s C_{pr}\text{Re}(Z_{r1})^2 \\ +\omega_s L_{pr}\left[[1 - \omega_s C_{pr}(\omega_s L_{\text{eq1}} + \text{Im}(Z_{r1}))]^2 + (\omega_s C_{pr}\text{Re}(Z_{r1}))^2\right] \end{array} \right\}}{\text{Re}(Z_{r1})} \tag{27}$$

TABLE II
PARAMETERS OF THE *LCC*-S SYSTEM

Parameter	Symbol	Value
Self-inductance of the primary coil	$L_{\rm p}$	92μH
Self-inductance of the secondary coil	$L_{\rm s}$	87.8μH
Series-compensated inductor in primary side	$L_{\rm pr}$	24.9μH
Series-compensated capacitor in primary side	$C_{\rm p}$	52.3nF
Series-compensated capacitor in secondary side	$C_{\rm s}$	40nF
Parallel-compensated capacitor in primary side	$C_{\rm pr}$	143.7nF
Coupling coefficient	k	0.22
Winding resistance of the primary coil	$R_{\rm p}$	49mΩ
Winding resistance of the secondary coil	$R_{\rm s}$	43mΩ
Input DC voltage	$V_{\rm in}$	300V
Load resistance	$R_{\rm L}$	26.2Ω

will occur around f_n too. Thus, a reasonable parameters design process is needed to avoid the frequency bifurcation. Since it is not the main research content in this article, it is assumed that the system has been designed appropriately without frequency bifurcation in this article.

Besides, in Fig. 5, the areas corresponding to $\angle Z_{\rm in1}>0$ and $\angle Z_{\rm in1}<0$ mean that $Z_{\rm in1}$ is inductive or capacitive, respectively. The necessary condition for ZVS operation is that $\angle Z_{\rm in1}$ locates in the inductive zone. It can be seen that the maximum of $\angle Z_{\rm in1}$ is closed to 90° in this area, which means the range of f_s is wide enough for ZVS operation within wide power range. In addition to this, harmonics in turn-OFF current contribute to achieving the ZVS operation as well.

B. Analysis of Power Characteristic

The characteristic of transmission power P_L against δ and f_s should be surveyed secondly. Since only fundamental component contributes to P_L, the relation among P_L^*, f_s, and δ is given as

$$P_L{}^* = \frac{P_L}{P_{\rm full-load}} = \frac{I_{\rm eq1}^2 {\rm Re}\left(Z_{\rm eq1}\right)}{\dfrac{8M^2U_{\rm in}^2}{\pi^2 {L_{pr}}^2 R_{\rm ac}}} \tag{28}$$

where $I_{\rm eq1}$ can be obtained by (14) and $Z_{\rm eq1}$ (i.e., $N=1$) is shown in Fig. 4. Based on (28) and parameters in Table II as an example, the variation tendency of P_L^* varies with f_s^* and δ under different coupling coefficient k is shown in Fig. 6, where the per-unit value P_L^* takes the rated power when $f_s=f_n$ and $\delta=0$ as the reference. Under the VFPS control, four DOF in Fig. 3 can be simplified to two DOF, i.e., f_s and δ.

It can be known that P_L^* is monotonic with f_s^* and δ, respectively, under different k and P_L^* is dominated by δ. Therefore, δ is used to adjust the transmission power and f_s is used to realize ZVS operation for further analysis. Besides, P_L^* increases with the decrease of δ, and slightly increases with the increase of f_s^* when f_s is around f_n.

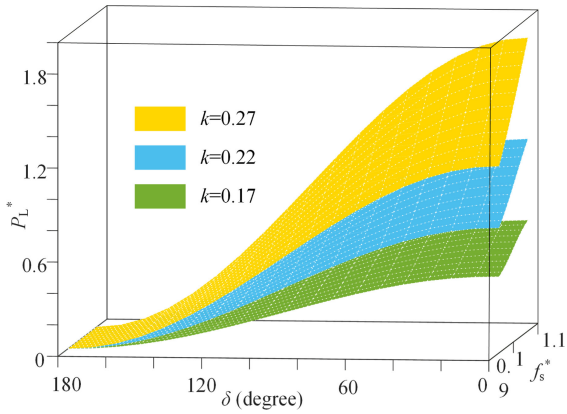

Fig. 6. Variation tendency for P_L^* against the f_s^* and δ with different k of *LCC*-S system.

C. Conditions for ZVS Operation

Except for the stability preconditions mentioned in part A and B, there are also some conditions need to be satisfied for ZVS operation.

Before power switches are turned ON, the parasitic capacitance of switches should be depleted in order to realize ZVS operation for the F-B inverter. There are four conditions to be met for ZVS operation, as given in (29) [34]

$$\begin{cases} i_{L_{pr}}\left(t_0\right) \le -I_{\rm th} \\ i_{L_{pr}}\left(t_1\right) \ge I_{\rm th} \\ i_{L_{pr}}\left(t_2\right) \ge I_{\rm th} \\ i_{L_{pr}}\left(t_3\right) \le -I_{\rm th} \end{cases} \tag{29}$$

where $I_{\rm th}$ is the threshold current and used to discharge these parasitic capacitors of power switches.

For convenient realization, (29) needs to be simplified. On the one hand, under the proposed optimal VFPS control, the input voltage $\boldsymbol{U_{pN}}$ in Fig. 3 is symmetrical, which means that if S_1 and S_3 can achieve ZVS operation, similarly so can S_2 and S_4. Thus, (29) is simplified as

$$\begin{cases} i_{L_{pr}}\left(t_0\right) \le -I_{\rm th} \\ i_{L_{pr}}\left(t_1\right) \ge I_{\rm th}. \end{cases} \tag{30}$$

On the other hand, by adding $i_{Lpr}(t_0)$ and $i_{Lpr}(t_1)$ from (23), (31) can be derived as

$$\boldsymbol{i_{L_{pr}}}\left(\boldsymbol{t}_0\right) + \boldsymbol{i_{L_{pr}}}\left(\boldsymbol{t}_1\right) = \left|{\rm Im}\left(\boldsymbol{U_{C_{eq1}}}\right)\right| \frac{2\sin\delta}{\sqrt{1+\cos\delta}} + \left|{\rm Im}\left(\boldsymbol{U_{C_{eq3}}}\right)\right| \frac{2\sin\left(3\delta\right)}{\sqrt{1+\cos\left(3\delta\right)}}. \tag{31}$$

According to (31), when $0 \le \delta < \pi/3$ or $2\,\pi/3 \le \delta < \pi$, (31) is nonnegative; when $\pi/3 \le \delta < 2\,\pi/3$, although the second term is negative, $|{\rm Im}\boldsymbol{U}_{Ceq3}|$ is far less than $|{\rm Im}\boldsymbol{U}_{Ceq1}|$, and thus (31)

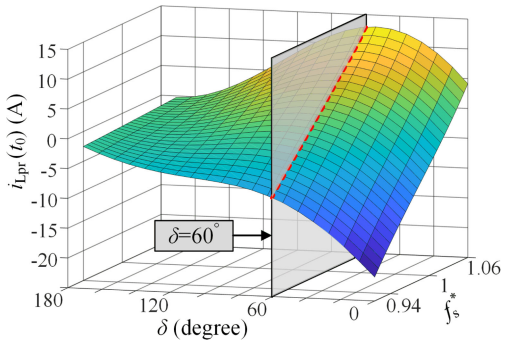

Fig. 7. Variation tendency for $i_{Lpr}(t_0)$ against f_s^* and δ.

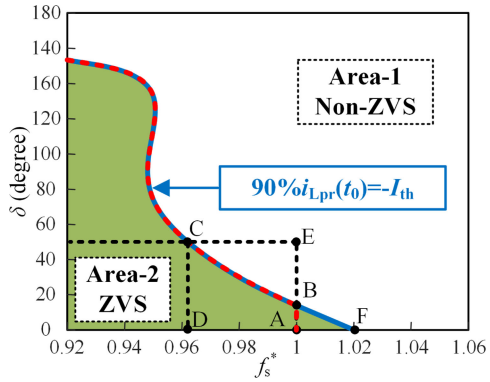

Fig. 8. Optimal working trajectory.

is still non-negative. Therefore, it can be known that in (30), if $i_{Lpr}(t_0) < -I_{\text{th}}$ is satisfied, $i_{Lpr}(t_1) > I_{\text{th}}$ must be satisfied too.

Thus, based on the analysis above, the four conditions in (29) can be simplified as one condition shown in (32), where a 10% margin is also taken in case the parameters drift occurs

$$90\% i_{L_{pr}}(t_0) \le -I_{\text{th}}. \tag{32}$$

D. Optimal Working Trajectory of ZVS Operation

The optimal working condition for ZVS operation is with minimum frequency variation, and the resonant tank maintains high efficiency within wide power range. After satisfying pre-conditions in Section IV-A–C, the ZVS operation can be realized steadily by adjusting f_s. However, it cannot realize the optimal operation by only satisfying (32). Thus, this part further proposes an optimal ZVS operation trajectory.

According to (32), it is known that the realization of ZVS depends on $i_{Lpr}(t_0)$. Thus, the variation tendency of $i_{Lpr}(t_0)$ against f_s and δ is investigated, as shown in Fig. 7.

As can be known in Fig. 7, no matter what δ is, f_s is always monotonous to $i_{Lpr}(t_0)$. For example, the red curve is generated by taking the intersection of the plane $\delta = 60°$ and the surface, where $i_{Lpr}(t_0)$ increases monotonously with f_s. Based on this characteristic, (32) can be easily satisfied by adjusting the value of f_s. In order to illustrate the adjustment more clearly, taking the intersection of the plane $90\% * i_{Lpr}(t_0) = -I_{\text{th}}$ and the surface in Fig. 7, the intersection curve is generated as shown in Fig. 8.

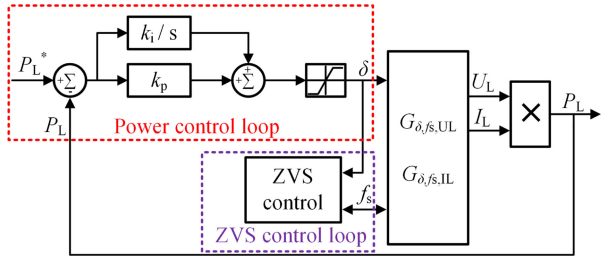

Fig. 9. Control block of *LCC*-S system.

In Fig. 8, Area-1 is the non-ZVS area where $90\%\ i_{Lpr}(t_0) > -I_{th}$ and (32) is dissatisfied; Area-2 is the ZVS area where $90\%\ i_{Lpr}(t_0) < -I_{\text{th}}$ and (32) is satisfied; the blue solid line is where $90\%\ i_{Lpr}(t_0) = -I_{\text{th}}$, i.e., the critical line of ZVS operation. Point A is the rated operation point under $f_s^* = 1$ and $\delta = 0°$. Because transfer efficiency decreases with the deviation between f_s and f_n, the red dotted line is the optimal working trajectory, which is under the minimum frequency variation.

To achieve optimal operation, the range of f_s variation needs to be minimum. Taking P_L decrease as an example, when rated P_L (corresponding to Point A) needs to be decreased, the operation point moves from point A vertically upward for minimum f_s variation (i.e., f_s is unchanged) with δ increasing. During this process, the operation point still locates in Area-2 and, thus, the F-B inverter remains ZVS operation. After reaching point B on the critical line, if P_L still needs to be decreased, in order to maintain ZVS operation and minimum f_s variation, the operation point then move along the red dotted line until finally reaching the desired operating point C. The analysis of P_L increasing is similar and, thus, is not repeated here.

As a result, by making the operation point stay on the desired trajectory, shown as red dotted line in Fig. 8, the optimal ZVS operation with high efficiency can be achieved.

E. VFPS Control Diagram

Based on the analysis of the optimal trajectory in Section IV-D, this part gives the realization of the proposed optimal VFPS control. The primary-side control diagram of the *LCC*-S system is given in Fig. 9, consisting of two parts: the power control loop and the ZVS control loop. The power control loop is the main control loop to guarantee that the system can transfer required power to load. Based on this power control, the ZVS control is added to realize the ZVS operation of the F-B inverter.

For power loop, the output power P_L is sampled and compared with the desired reference P_L^*; the difference between them is then sent as the input of the PI controller; the output of the PI controller is sent to the F-B inverter as the phase angle δ; by adjusting δ, P_L can finally track to P_L^*.

For ZVS loop, f_s and δ at current control cycle are acquired to obtain $i_{Lpr}(t_0)$ based on (23); according to the monotonicity between $i_{Lpr}(t_0)$ and f_s analyzed in Section IV-D, f_s is adjusted by Δf, which is selected as 50 Hz in this article considering the response time and system oscillation; then this value is set as the switching frequency at next control cycle; by modifying f_s,

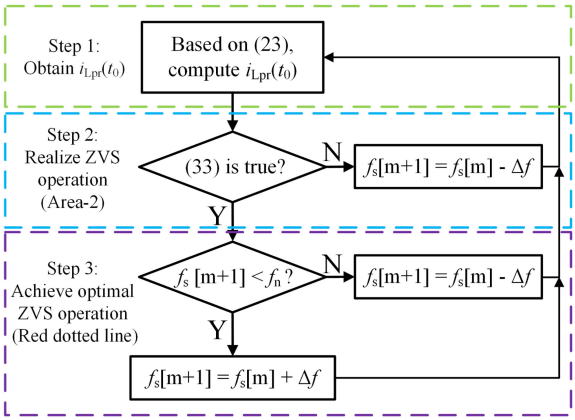

Fig. 10. Flowchart of the ZVS control block.

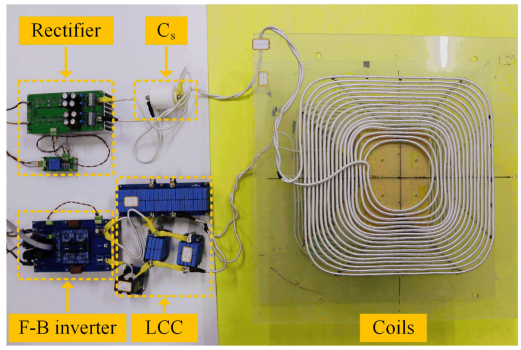

Fig. 11. Experimental prototype.

the working trajectory is finally located on the red dotted line in Fig. 8, which is the optimal working trajectory. Due to the large data volumes, which is four-dimensional (i.e., f_s, δ, k, and R_L), the look-up table method is not recommended in this article.

To achieve automatic operation, the flowchart of ZVS loop is further designed, as shown in Fig. 10, where following three steps are contained.

Step 1: At the beginning, the original f_s is set as the resonant frequency f_n, and the instantaneous $i_{Lpr}(t_0)$ is calculated based on (23).

Step 2: Based on the calculated $i_{Lpr}(t_0)$, the controller judges whether (32) is true or not. Combining with Fig. 8, if (32) is false, the system is working under non-ZVS operation as shown in Area-1, and f_s should be decreased by Δf (f_s[m] and f_s[m + 1] are the switching frequencies at present and next control interrupt, respectively) until the operation point reaches Area-2; if (32) is true, the system is working under ZVS operation as shown in Area-2, and thus the process moves to the next step.

Step 3: Even if (32) is satisfied, which means power switches have already been in ZVS operation, this frequency is probably not the optimal one if the operation point is not on the desired working trajectory, and f_s needs to be adjusted based on the following principle: the deviation between f_s and f_n needs to be minimum. Thus, f_s needs to compare with f_n, if f_s is larger than f_n such as the region ABF in Fig. 8, f_s should be decreased by Δf until it reaches to f_n. If f_s is smaller than f_n such as the region ABCD in Fig. 8, f_s needs to be increased by Δf until it reaches to the red dotted line. Finally, the ZVS operation with minimum frequency variation is achieved.

For example, assume that when P_L changes, the variation of δ is 0–50°, and in order to simplify the explanation, the influence of f_s on P_L is neglected. The operation trajectories under different situations are analyzed as follows.

1) If PS control is adopted, when P_L decrease, the operation trajectory is A-B-E as shown in Fig. 8, and B-E is located in the non-ZVS area.
2) If VFPS control is adopted without step 3, when P_L decrease, the operation trajectory is A-B-C; however, when P_L increase, the operation trajectory is C-D. The frequency of point D is smaller than f_n, which decreases the efficiency.
3) If VFPS control is adopted without the frequency limiting f_n, when P_L increase, the operation trajectory is C-B-F. The frequency of point F is larger than f_n, which decreases the efficiency.

Consequently, adopting the proposed flowchart in Fig. 10, the system can realize ZVS operation located in the optimal working trajectory within wide power range.

V. Experimental Verification

A. System Setup

To verify the accuracy of above analysis and feasibility of the proposed optimal VFPS control strategy, a 2.2-kW *LCC*-S compensated IPT experimental prototype is built up, as shown in Fig. 11. It mainly consists of a dc source, a high-frequency F-B inverter, a *LCC*-S resonant network, an F-B rectifier, and a resistance load; and the specifications are given in Table II. The parameters are designed appropriately to guarantee high efficiency of the system and avoid frequency bifurcation around f_n. The F-B inverter is controlled by TMS320F28335, and the power switches used in this inverter are Infineon high speed power MOSFET IPW65R041CFD. The rectifier diodes in secondary side are DSEP60-06A.

Due to the large output capacitance of the MOSFETs, the current for ZVS operation in switching moments is approximately 2.7 A, which means $I_{\rm th} = 2.7$ A, and according to (32), the design value of switching-moment current for ZVS operation is 3 A.

B. Verification of the Harmonic-Considered Universal Time-Domain Model

In order to verify the accuracy of the proposed harmonic-considered model in Section III, the experimental and calculated waveforms of four tests are compared in Fig. 12(a)–(d), respectively. Parameters of tests are shown in Table III.

To verify the universality of the proposed harmonic-considered time-domain model, the experiment conditions of four tests are different, given as follows: test 1 is under full

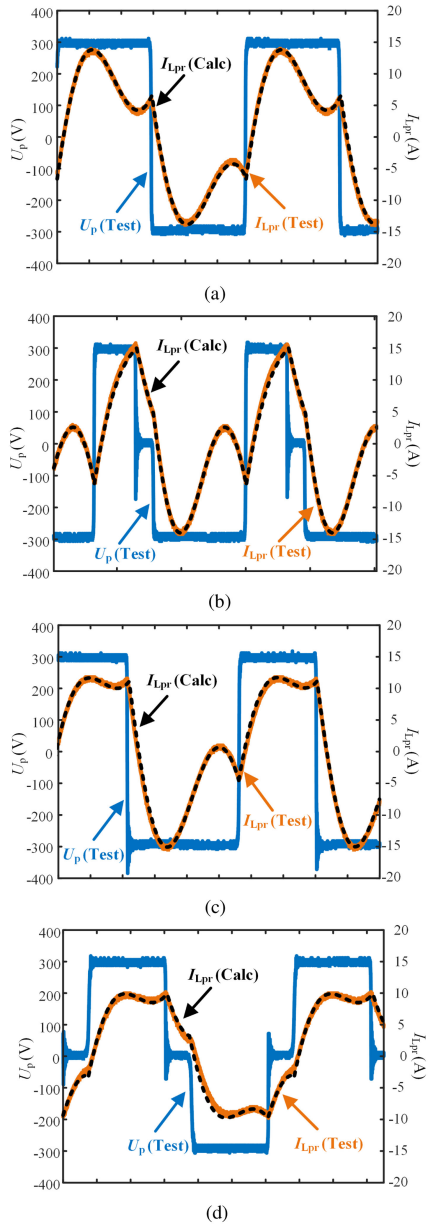

Fig. 12. Waveforms of test 1–4. (a) Test 1 under full duty cycle control. (b) Test 2 under AVS control. (c) Test 3 under ADS control. (d) Test 4 under proposed optimal VFPS control.

duty cycle control with $f_s = f_n$ and symmetrical pulsewidth of the F-B inverter, and outputs the rated power; test 2 is under AVC control with $f_s = f_n$ and asymmetrical pulsewidth of the F-B inverter; test 3 is under ADC control with $f_s = f_n$ and symmetrical pulsewidth of the F-B inverter; test 4 is under the proposed optimal VFPS control with symmetrical pulsewidth of the F-B inverter, and f_s is unequal to f_n.

As can be seen in Fig. 12, the blue line is the measured waveform of $u_p(t)$, and the orange line is the measured waveform of $i_{Lpr}(t)$. The black dotted line is the calculated waveform of $i_{Lpr}(t)$ using the universal time-domain model proposed above. The measured waveforms are in good agreement with the calculated waveforms. Negligible error exits, which is caused by the dead time of the F-B inverter and the neglect of loss resistance; however, the proposed harmonic-considered universal time-domain model is still accurate enough to analyze the *LCC*-S system.

TABLE III
VALUE OF CONTROL PARAMETERS IN FOUR TESTS

Parameter	Test 1	Test 2	Test 3	Test 4
f_s	85kHz	85kHz	85kHz	82.2kHz
α	180°	140°	150°	180°
β	180°	260°	210°	180°
δ	0°	40°	0°	40°
Modulation	Full duty cycle	AVC	ADC	VFPS

Consequently, the four tests verify the accuracy and universality of proposed model. It is not only suitable for asymmetrical and symmetrical pulse systems, but also VF systems.

C. Verification of the Optimal VFPS Control Strategy

To verify the validity of the proposed optimal VFPS control strategy, two groups of contrast closed-loop experiments are carried out. One is the steady-state contrast experiments with the PS control, the VFPS control based on the FHA method, and the proposed optimal VFPS control based on the harmonic-considered model, respectively. The other is experiment of dynamic process when PS control turns into the proposed optimal VFPS control.

1) Steady-State Contrast Experiments: The ZVS operation with three control strategies (i.e., PS control, VFPS control based on FHA method, and the proposed optimal VFPS control) at 1/8 rated load, 3/8 rated load, 5/8 rated load, and 7/8 rated load are compared, respectively. The differences among these three control strategies are as follows.

1) PS control adjusts the phase between the leading leg and the lagging leg of the inverter for output power control.
2) VFPS control based on the FHA method, according to the calculated turn-OFF current that is based on the time-domain model of the fundamental harmonic, adjusts the switching frequency to realize ZVS operation. Meanwhile the system adjusts the phase between two legs of the inverter to control the output power.
3) The proposed optimal VFPS control based on the harmonic-considered model. The differences between the proposed optimal VFPS control and the VFPS control based on FHA method are reflected in the following two aspects.

a) The first is the calculation method of the turn-OFF current. The calculation method in this article is based on the proposed harmonic-considered model of LCC-S topology, which is more accurate to calculate the turn-OFF current.
b) The second is the deviation of the switching frequency within wide power range. With the accurate turn-OFF current and well-designed control, the frequency deviation (between the switching frequency and resonant frequency) is minimum, which ensures high efficiency of the resonant tank.

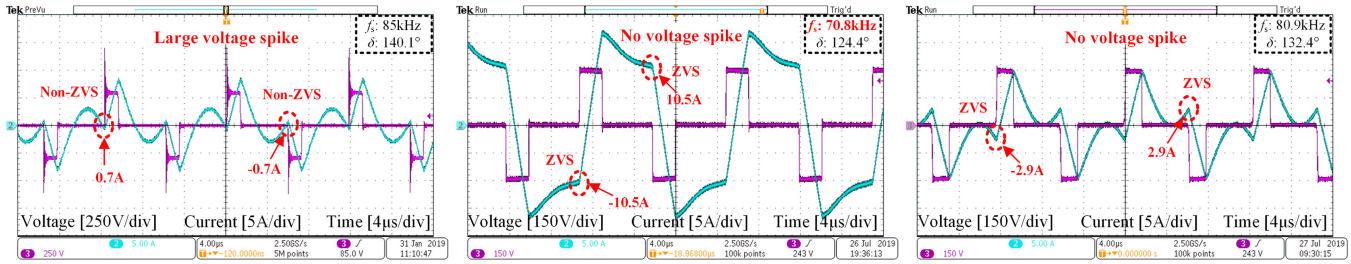

(a) (b) (c)

Fig. 13. Waveforms of u_p and i_{Lpr} at 1/8 rated load with (a) PS control, (b) VFPS control based on FHA method, and (c) proposed optimal VFPS control.

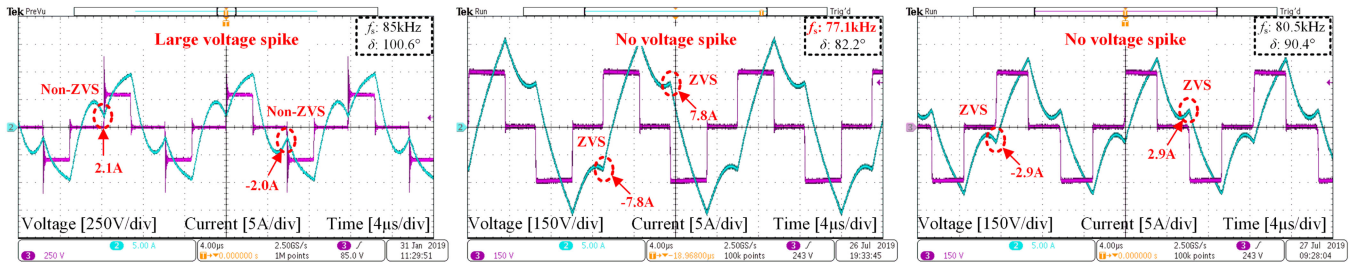

(a) (b) (c)

Fig. 14. Waveforms of u_p and i_{Lpr} at 3/8 rated load with (a) PS control, (b) VFPS control based on FHA method, and (c) proposed optimal VFPS control.

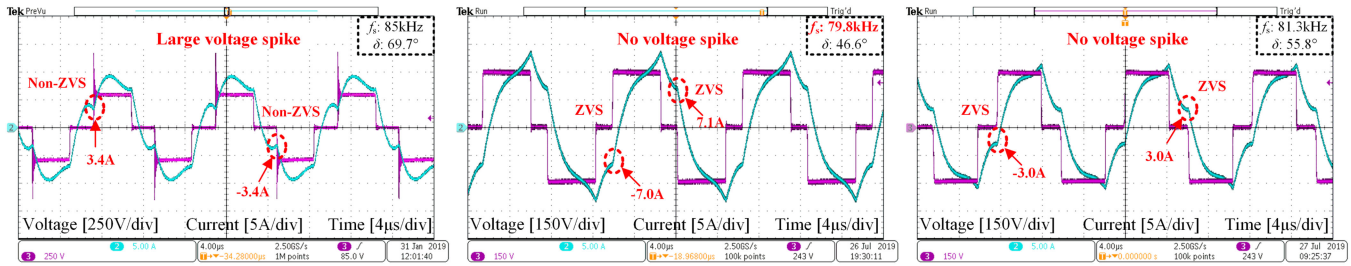

(a) (b) (c)

Fig. 15. Waveforms of u_p and i_{Lpr} at 5/8 rated load with (a) PS control, (b) VFPS control based on FHA method, and (c) proposed optimal VFPS control.

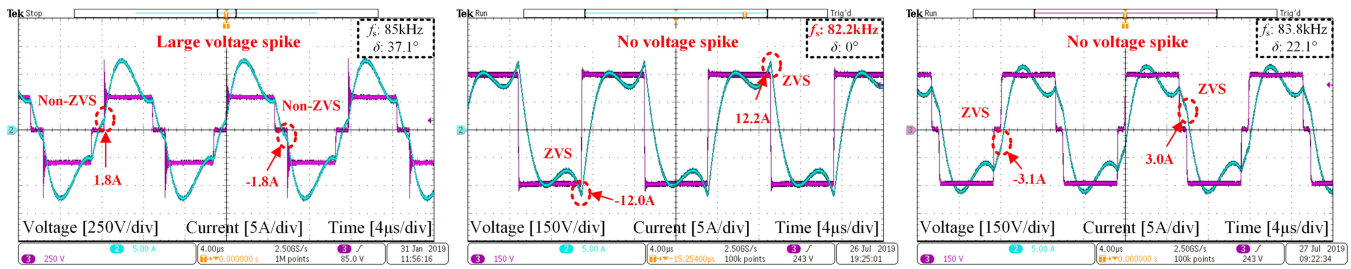

(a) (b) (c)

Fig. 16. Waveforms of u_p and i_{Lpr} at 7/8 rated load with (a) PS control, (b) VFPS control based on FHA method, and (c) proposed optimal VFPS control.

The waveforms of u_p and i_{Lpr} of the F-B inverter at 1/8 rated load, 3/8 rated load, 5/8 rated load, and 7/8 rated load are shown in Figs. 13–16, respectively.

As can be seen from Figs. 13–16, the inverter suffers hard-switching operation with PS control, which results in a large voltage spike in u_p. Besides, the inverter can realize ZVS operation with either the VFPS control based on FHA method or the proposed optimal VFPS control. However, the variation of the switching frequency with the VFPS control based on FHA method is wide, especially in light load condition, which is not

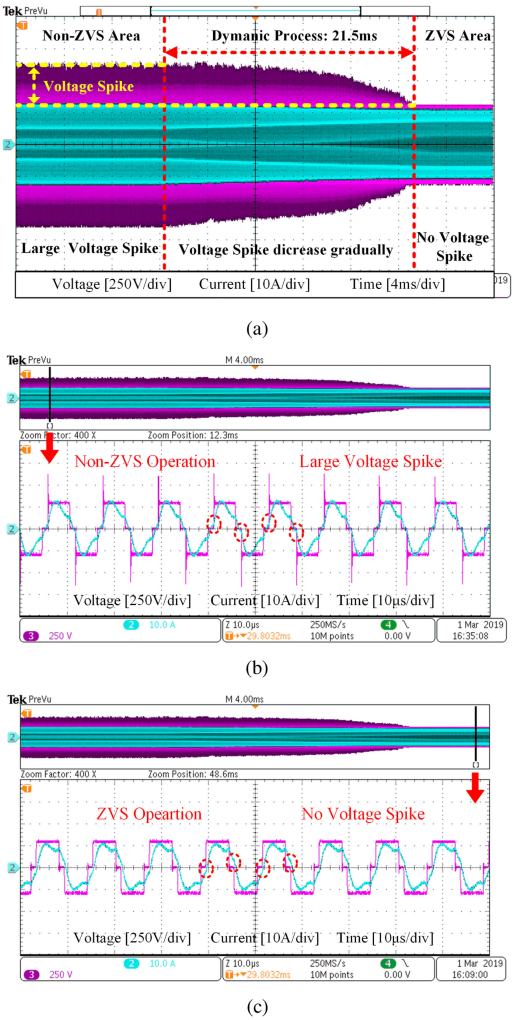

Fig. 17. Dynamic waveforms at 7/8 load. (a) Entire dynamic process. (b) Detail waveforms under PS control. (b) Detail waveforms under proposed VFPS control.

optimal and leads to poor efficiency of the resonant tank. On the contrary, the switching frequency variation with the proposed optimal VFPS control is minimum because the turn-OFF current at different rated load is closed to the set value.

It is noting that in Fig. 13(c), even if the waveform exists two zero crossing points before the switching transitions taking place, the system can still achieve ZVS operation. In Fig. 16(b), although δ is zero, the switching frequency is less than 85 kHz and the power is about in 7/8 rated load.

Consequently, the proposed optimal VFPS control can realize the optimal ZVS operation within wide power range in *LCC*-S topology. The contrast experiments verify the validity of the proposed optimal VFPS control.

2) Dynamic Waveforms: The following experimental waveforms in Fig. 17 are the dynamic process at 7/8 rated load. The initial control strategy is PS control, and after a while, the proposed optimal VFPS control is adopted. Fig. 17(a) is the entire dynamic process from PS control to VFPS control. Fig. 17(b) and (c) are the detail waveforms under PS control and proposed VFPS control, respectively.

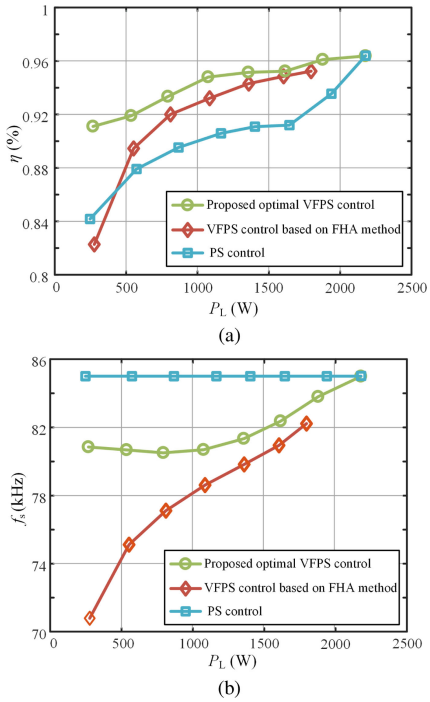

Fig. 18. System efficiency and switching frequency comparison with three control strategies. (a) Efficiency comparison. (b) Switching frequency comparison.

As can be seen in Fig. 17(a), before the VFPS control is adopted, the F-B inverter works with hard-switching operation, and the voltage spike exceeds 600 V, which may damage power switches. Once the proposed optimal VFPS control is enabled, the F-B inverter turns into ZVS operation after 21.5-ms dynamic process with $\Delta f = 50$ Hz, which is acceptable in IPT system

D. Efficiency Comparison

The dc to dc efficiency curves and the switching frequency comparison with three control strategies are shown in Fig. 18. As can be seen from Fig. 18, the following conclusions can be obtained.

1) The rated power is 2.2 kW and a peak efficiency of 96.4% is achieved with $k = 0.22$.
2) The efficiency with the PS control drops rapidly when power decreases, with efficiency decrease of 2.6%–6.9% than the one adopted the proposed optimal VFPS control. The reason is that inverter suffers hard-switching operation with the PS control, which leads to a poor efficiency.
3) The efficiency with the VFPS control based on FHA method drops rapidly in light load with efficiency decrease of 0.8%–8.8% than the one adopted the proposed optimal VFPS control, even if these experiments can realize ZVS operation. The reason is that the frequency deviation in light load is wide with the VFPS control based on FHA method, which leads to a poor efficiency.
4) The efficiency with the proposed optimal VFPS control maintains high level within wide power range, which is attributed to the ZVS operation and the minimum frequency deviation.

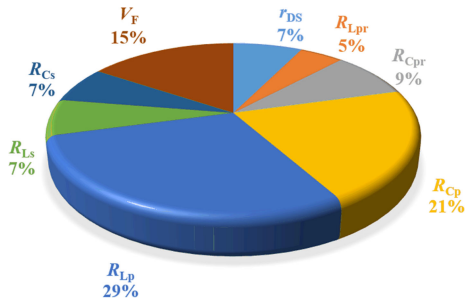

Fig. 19. Various losses of the *LCC*-S IPT system.

The loss parameters of each component in *LCC*-S system can be obtained in the data book. The losses are calculated theoretically and listed in Fig. 19. Fig. 19 depicts various losses of the *LCC*-S IPT system in the full load condition. When the output power is 2.2 kW, the calculated power dissipation of the inverter is 5.3 W, which is relatively small compared with other losses because of the ZVS operation. The drain-source on-state resistance of MOSFET used in this article is relatively small. The greatest loss is 20.8 W (29%) in L_p, and the second one is 15.2 W (21%) in C_p. Due to the large current in primary-side coil, the losses in L_P and C_p are relatively large compared with 4.9 W in L_s and 4.9 W in C_s. In addition, the losses in L_{pr}, C_{pr}, and rectifier diode are 3.3, 6.2, and 11.2 W, respectively.

VI. Conclusion

In order to realize ZVS operation of the *LCC*-S topology within wide power range, this article proposes an optimal VFPS control strategy. The universal harmonic-considered time-domain model of the *LCC*-S system is obtained, which takes high-order harmonics of power switches current into consideration. And it is not only suitable for the symmetrical and asymmetrical pulse control, but also for the VF control. Based on this model, the switching-moment current of power switches can be calculated accurately. By comparing it with the ZVS criterion and adopting proper logic procedure, the controller adjusts the switching frequency to achieve ZVS operation with minimum frequency variation. With the proposed control, the efficiency of the F-B inverter within wide power range is improved by ZVS operation and the resonant tank maintains high efficiency by operation with the minimum frequency variation.

In the experiment part, a 2.2-kW IPT prototype is built. The measured waveforms are in good agreement with the calculated waveforms under different control strategies, which verify the accuracy of the proposed time-domain model. Moreover, the results of contrast experiments show good agreement with the theoretical analysis. Switches in the F-B inverter can realize the optimal ZVS operation within wide power range with a peak efficiency of 96.4%. The efficiency with proposed optimal VFPS control strategy is 2.6%–6.9% higher than the one adopted PS control due to its soft-switching realization and 0.8%–8.8% higher than the one adopted VFPS control based on FHA method due to the minimum frequency variation.

References

[1] P. Si, A.P. Hu, S. Malpas, and D. Budgett, "A frequency control method for regulating wireless power to implantable devices," *IEEE Trans. Biomed. Circuits Syst.*, vol. 2, no. 1, pp. 22–29, Mar. 2008.

[2] Q. Chen, S.C. Wong, C.K. Tse, and X. Ruan, "Analysis, design, and control of a transcutaneous power regulator for artificial hearts," *IEEE Trans. Biomed. Circuits Syst.*, vol. 3, no. 1, pp. 23–31, Feb. 2009.

[3] X. Liu and S.Y. Hui, "Simulation study and experimental verification of a universal contactless battery charging platform with localized charging features," *IEEE Trans. Power Electron.*, vol. 22, no. 6, pp. 2202–2210, Nov. 2007.

[4] M. R. Basar, M. Y. Ahmad, J. Cho, and F. Ibrahim, "An improved wearable resonant wireless power transfer system for biomedical capsule endoscope," *IEEE Trans. Ind. Electron.*, vol. 65, no. 10, pp. 7772–7781, Oct. 2018.

[5] D. Liu and S.V. Georgakopoulos, "Cylindrical misalignment insensitive wireless power transfer systems," *IEEE Trans. Power Electron.*, vol. 33, no. 11, pp. 9331–9343, Nov. 2018.

[6] H. Feng, T. Cai, S. Duan, X. Zhang, H. Hu, and J. Niu, "A dual-side-detuned series–series compensated resonant converter for wide charging region in a wireless power transfer system," *IEEE Trans. Ind. Electron.*, vol. 65, no. 3, pp. 2177–2188, Mar. 2018.

[7] T. Z. Kan, R. K. Mai, P. P. Mercier, and C. Mi, "A three-phase wireless charging system for lightweight autonomous underwater vehicles," in *Proc. Annu. IEEE Appl. Power Electron. Conf. Expo.*, 2017, pp. 1407–1411.

[8] T. Kan, R. Mai, P. P. Mercier, and C. C. Mi, "Design and analysis of a three-phase wireless charging system for lightweight autonomous underwater vehicles," *IEEE Trans. Power Electron.*, vol. 33, no. 8, pp. 6622–6632, Aug. 2018.

[9] T. Orekan, P. Zhang, and C. Shih, "Analysis, design, and maximum power-efficiency tracking for undersea wireless power transfer," *IEEE Trans. Emerg. Sel. Topics Power Electron.*, vol. 6, no. 2, pp. 843–854, Jun. 2018.

[10] M. Kim, D. Joo, and B.K. Lee, "Design and control of inductive power transfer system for electric vehicles considering wide variation of output voltage and coupling coefficient," *IEEE Trans. Power Electron.*, vol. 34, no. 2, pp. 1197–1208, Feb. 2019.

[11] H. Feng, T. Cai, S. Duan, J. Zhao, X. Zhang, and C. Chen, "An LCC-compensated resonant converter optimized for robust reaction to large coupling variation in dynamic wireless power transfer," *IEEE Trans. Ind. Electron.*, vol. 63, no. 10, pp. 6591–6601, Oct. 2016.

[12] L. Zhao, D. J. Thrimawithana, U. K. Madawala, A. P. Hu, and C.C. Mi, "A misalignment-tolerant series-hybrid wireless EV charging system with integrated magnetics," *IEEE Trans. Power Electron.*, vol. 34, no. 2, pp. 1276–1285, Feb. 2019.

[13] C. C. Mi, G. Buja, S.Y. Choi, and C. T. Rim, "Modern advances in wireless power transfer systems for roadway powered electric vehicles," *IEEE Trans. Ind. Electron.*, vol. 63, no. 10, pp. 6533–6545, Oct. 2016.

[14] J. Zhao, T. Cai, S. Duan, H. Feng, C. Chen, and X. Zhang, "A general design method of primary compensation network for dynamic wpt system maintaining stable transmission power," *IEEE Trans. Power Electron.*, vol. 31, no. 12, pp. 8343–8358, Dec. 2016.

[15] Y. Su, L. Chen, X. Wu, A. P. Hu, C. Tang, and X. Dai, "Load and mutual inductance identification from the primary side of inductive power transfer system with parallel-tuned secondary power pickup," *IEEE Trans. Power Electron.*, vol. 33, no. 11, pp. 9952–9962, Nov. 2018.

[16] X. Dai, X. Li, Y. Li, and A. P. Hu, "Maximum efficiency tracking for wireless power transfer systems with dynamic coupling coefficient estimation," *IEEE Trans. Power Electron.*, vol. 33, no. 6, pp. 5005–5015, Jun. 2018.

[17] Z. Huang, S. Wong, and C. K. Tse, "Control design for optimizing efficiency in inductive power transfer systems," *IEEE Trans. Power Electron.*, vol. 33, no. 5, pp. 4523–4534, May 2018.

[18] Y. Jiang, L. Wang, Y. Wang, J. Liu, X. Li, and G. Ning, "Analysis, design, and implementation of accurate ZVS angle control for EV battery charging in wireless high-power transfer," *IEEE Trans. Ind. Electron.*, vol. 66, no. 5, pp. 4075–4085, May 2019.

[19] C. S. Tang, Y. Sun, Y. G. Su, S. K. Nguang, and A. P. Hu, "Determining multiple steady-state ZCS operating points of a switch-mode contactless power transfer system," *IEEE Trans. Power Electron.*, vol. 24, no. 2, pp. 416–425, Feb. 2009.

[20] K. Song, Z. Li, Z. Du, G. Wei, and C. Zhu, "Design for constant output voltage and current controllability of primary side controlled wireless power transfer system," in *Proc. IEEE PELS Workshop Emerg. Technol., Wireless Power Transfer*, 2017, pp. 1–6.

[21] G. Buja, M. Bertoluzzo, and K. N. Mude, "Design and experimentation of WPT charger for electric city car," *IEEE Trans. Ind. Electron.*, vol. 62, no. 12, pp. 7436–7447, Dec. 2015.
[22] D. S. Oliveira and I. Barbi, "A three-phase ZVS PWM DC/DC converter with asymmetrical duty cycle for high power applications," *IEEE Trans. Power Electron.*, vol. 20, no. 2, pp. 370–377, Mar. 2005.
[23] M. B. Borage, K. V. Nagesh, M. S. Bhatia, and S. Tiwari, "Characteristics and design of an asymmetrical duty-cycle-controlled LCL-T resonant converter," *IEEE Trans. Power Electron.*, vol. 24, no. 10, pp. 2268–2275, Oct. 2009.
[24] J. M. Burdio, L. A. Barragan, F. Monterde, D. Navarro, and J. Acero, "Asymmetrical voltage-cancellation control for full-bridge series resonant inverters," *IEEE Trans. Power Electron.*, vol. 19, no. 2, pp. 461–469, Mar. 2004.
[25] L. A. Barragan, J. M. Burdio, J. I. Artigas, D. Navarro, J. Acero, and D. Puyal, "Efficiency optimization in ZVS series resonant inverters with asymmetrical voltage-cancellation control," *IEEE Trans. Power Electron.*, vol. 20, no. 5, pp. 1036–1044, Sep. 2005.
[26] K. Yan, Q. Chen, J. Hou, X. Ren, and X. Ruan, "Self-oscillating contactless resonant converter with phase detection contactless current transformer," *IEEE Trans. Power Electron.*, vol. 29, no. 8, pp. 4438–4449, Aug. 2014.
[27] L. Xu, Q. Chen, X. Ren, S. Wong, and C.K. Tse, "Self-oscillating resonant converter with contactless power transfer and integrated current sensing transformer," *IEEE Trans. Power Electron.*, vol. 32, no. 6, pp. 4839–4851, Jun. 2017.
[28] Y. Jiang, L. Wang, Y. Wang, J. Liu, M. Wu, and G. Ning, "Analysis, design and implementation of WPT system for EV's battery charging based on optimal operation frequency range," *IEEE Trans. Power Electron*., vol. 34, no. 7, pp. 6890–6905, Jul. 2019.
[29] V. Esteve *et al.*, "Improving the efficiency of IGBT series-resonant inverters using pulse density modulation," *IEEE Trans. Ind. Electron.*, vol. 58, no. 3, pp. 979–987, Mar. 2011.
[30] N. A. Ahmed, "High-frequency soft-switching AC conversion circuit with dual-mode PWM/PDM control strategy for high-power IH applications," *IEEE Trans. Ind. Electron.*, vol. 58, no. 4, pp. 1440–1448, Apr. 2011.
[31] Y. Fang and B. M. H. Pong, "Multiple harmonics analysis for variable frequency asymmetrical pulsewidth-modulated wireless power transfer systems," *IEEE Trans. Ind. Electron.*, vol. 66, no. 5, pp. 4023–4030, May 2019.
[32] Q. Chen, S. C. Wong, C. K. Tse, and X. Ruan, "Analysis, design, and control of a transcutaneous power regulator for artificial hearts," *IEEE Trans. Biomed. Circuits Syst.*, vol. 3, no. 1, pp. 23–31, Feb. 2009.
[33] M. Bojarski, E. Asa, K. Colak, and D. Czarkowski, "Analysis and control of multiphase inductively coupled resonant converter for wireless electric vehicle charger applications," *IEEE Trans. Transp. Electrific.*, vol. 3, no. 2, pp. 312–320, Jun. 2017.
[34] X. Zhang *et al.*, "A control strategy for efficiency optimization and wide ZVS operation range in bidirectional inductive power transfer system," *IEEE Trans. Ind. Electron.*, vol. 66, no. 8, pp. 5958–5969, Aug. 2019.
[35] X. Zhang, T. Cai, S. Duan, H. Feng, H. Hu, and J. Niu, "A harmonic-considered time domain model of LCC compensated wireless power transfer systems," in *Proc. IEEE Int. Power Electron. Appl. Conf. Expo.*, 2018, pp. 1–5.

Hongsheng Hu received the B.S. degree in electrical engineering from the Huazhong University of Science and Technology, Wuhan, China, in 2014, where he is currently working toward the Ph.D. degree with the School of Electrical and Electronics Engineering.

His research interests include wireless power transfer and magnetic design.

Tao Cai received the Ph.D. degree in control science and engineering from the Huazhong University of Science and Technology, Wuhan, China, in 2004.

He is currently with the Huazhong University of Science and Technology. He has authored or coauthored about 20 technical papers published in journals and conference proceedings. His current research interests include advanced signal processing and energy management of renewable power generation.

Shanxu Duan (SM'16) received the B.S., M.S., and Ph.D. degrees in electrical engineering from the Huazhong University of Science and Technology, Wuhan, China, in 1991, 1994, and 1999, respectively.

Since 1991, he has been a Faculty Member with the College of Electrical and Electronics Engineering, Huazhong University of Science and Technology, where he is currently a Professor. His research interests include stabilization, nonlinear control with application to power electronic circuits and systems, fully digitalized control techniques for power electronics apparatus and systems, and optimal control theory and corresponding application techniques for high-frequency pulsewidth modulation power converters.

Dr. Duan is a Senior Member of the Chinese Society of Electrical Engineering and a Council Member of the Chinese Power Electronics Society. He was selected as one of the New Century Excellent Talents by the Ministry of Education of China in 2007. He was also the recipient of the honor of "Delta Scholar" in 2009.

Xiaoming Zhang received the B.S. degree in electrical engineering and automation from the Huazhong University of Science and Technology, Wuhan, China, in 2014, where he is currently working toward the Ph.D. degree with the School of Electrical and Electronics Engineering.

His research interests include wireless power transmission and power electronics applied to electric vehicles.

Jintao Niu received the B.S. degree in water conservancy and hydropower engineering and M.S. degree in electrical engineering from the Huazhong University of Science and Technology, Wuhan, China, in 2016 and 2019.

His research interests include high-power battery charger and energy management system.

Hao Feng (M'19) received the B.S. degree in control engineering and Ph.D. degrees in electrical engineering from the Huazhong University of Science and Technology, Wuhan, China, in 2013 and 2018, respectively.

Since 2018, he has been with the Future Renewable Electric Energy Delivery and Management Systems Center, Department of Electrical and Computer Engineering, North Carolina State University, as Postdoctoral Researcher. His research interests include inductive power transfer systems, bidirectional dc–dc converters, and medium voltage power conversion.